IOP Publishing Phys. Med. Biol. 65 (2020) 015002 (16pp) https://doi.org/10.1088/1361-6560/ab5bc6

Physics in Medicine & Biology

IPEM Institute of Physics and Engineering in Medicine

PAPER

RECEIVED
7 June 2019

REVISED
20 November 2019

ACCEPTED FOR PUBLICATION
26 November 2019

PUBLISHED
10 January 2020

Optimized sampling for high resolution multi-pinhole brain SPECT with stationary detectors

Yuan Chen[1,4], **Marlies C Goorden**[1], **Brendan Vastenhouw**[2,3] **and Freek J Beekman**[1,2,3]

[1] Section Biomedical Imaging, Delft University of Technology, Delft, The Netherlands
[2] MILabs B.V., Utrecht, The Netherlands
[3] Department of Translational Neuroscience, Brain Center Rudolf Magnus, University Medical Center Utrecht, Utrecht, The Netherlands
[4] Author to whom correspondence should be addressed.

E-mail: y.chen-4@tudelft.nl

Keywords: brain perfusion SPECT, sampling, multi-pinhole collimation, fast dynamic SPECT, bed translation

Abstract

Brain perfusion SPECT can be used in the diagnosis of various neurologic or psychiatric disorders, e.g. stroke, epilepsy, dementia and posttraumatic stress disorder. As traditional SPECT provides limited resolution and sensitivity, we recently proposed a high resolution focusing multi-pinhole clinical SPECT scanner dubbed G-SPECT-I (Beekman *et al* 2015, *Eur. J. Nucl. Med. Mol. Imaging* **42** S209). G-SPECT-I achieves data completeness in the scan region of interest (ROI) by making small translations of the patient bed while using projections from all bed positions together for image reconstruction. A strategy to restrict the number of bed translations is desired to minimize overhead time. Previously we presented optimized bed translation paths for focused partial brain imaging, while here we focus on whole brain imaging which is the common procedure in perfusion studies. Thus, a series of noise-free scans using a reduced number of bed positions were simulated and compared to an oversampled reference scan acquired with 128 bed positions. Noisy simulations were included to validate the utility of the optimized sequences in more realistic situations. Brain uptake ratios (BURs) and left–right Asymmetry Indices (AIs) in 51 selected regions of interest (ROIs) were calculated for assessment. Results show that images were barely affected by decreasing the number of bed positions from 128 down to 18 (mean deviation from the reference of only 2.2% and 1.5% for the BUR and AI, respectively) while slightly larger deviations (2.9% and 2.7%, respectively) were obtained when using 12 positions. For both 18- and 12-position sequences these deviations due to sampling were much smaller than those induced by noise (mean deviation of 6.5% and 8.6%, respectively). Given an associated total overhead for bed movement of half a minute (18 positions) or 20 s (12 positions), G-SPECT-I can be a clinical platform that brings new protocols for fast (dynamic) whole brain SPECT and motion correction into reach.

1. Introduction

Brain SPECT with ^{99m}Tc, e.g. with ^{99m}Tc-HMPAO or ^{99m}Tc-ECD, has a widely demonstrated utility in detecting regional cerebral blood flow and in indirectly measuring neuronal activity. This enables the noninvasive assessment of cerebrovascular disease (e.g. stroke) and neurological dysfunction (e.g. epilepsy, dementias) (Catafau 2001, Juni *et al* 2009). In particular, SPECT is the only imaging modality practically capable to perform an ictal scan during epileptic seizures due to the 'snapshot' property of the tracers in use (Knowlton 2006, Kim and Mountz 2011). Besides these clinically well-established applications, additional indications in the psychiatric domain are currently under active evaluation (Camargo 2001, Amen *et al* 2011, Santra and Kumar 2014), for example in post-traumatic stress disorder, anxiety and depression (Amen *et al* 2009, Amen 2015).

Presently general purpose single-, dual- or triple-head SPECT scanners provide a limited spatial resolution of 7–10 mm, with sensitivity in the range of ~100–250 cps/MBq. Some dedicated brain SPECT scanners, e.g. CeraSPECT, inSpira HD or NeuroFocus (Stoddart and Stoddart 1992, Fakhri *et al* 2006, Sensakovic *et al* 2014, Stam *et al* 2018), have been developed, but resolutions are still around 7 mm and some are not manufactured

anymore. Such a limited resolution hampers detection of small localized perfusion abnormalities which can compromise accuracy of diagnosis and early detection of neuropathology while a low sensitivity requires a relatively high tracer dose and long scanning time resulting in patient discomfort as well as increased risk of motion artefacts. These limited resolution-sensitivity tradeoffs of previous SPECT scanners are due to the conventional collimator designs, a limited number of detectors or restricted detector surface area, lack of image magnification, etc.

Recently, efforts have been made to develop brain SPECT systems based on multi-pinhole collimation owing to its enhanced resolution-sensitivity tradeoff especially when imaging small objects. Simulation studies have been carried out to optimize multi-pinhole systems (Van Audenhaege *et al* 2011, 2013, King *et al* 2012, Mukherjee *et al* 2014, Chen *et al* 2017), however only a few systems have been built and/or acquired physical scans (Lee *et al* 2014, Beekman *et al* 2015). Our group initially developed various focused multi-pinhole SPECT systems for preclinical purposes, e.g. U-SPECT-I, U-SPECT-II, VECTor, U-SPECT^{+} (Beekman 2005, van der Have *et al* 2009, Goorden *et al* 2013, Ivashchenko *et al* 2015), and lately this technology was translated in a prototype system named G-SPECT-I for clinical applications (Beekman *et al* 2015). The preclinical systems achieve sub-half-millimeter SPECT resolution and sub-second-frame dynamic scans for small animals (Befera *et al* 2014, Ivashchenko *et al* 2014, 2015) and are now in use in labs worldwide. The G-SPECT-I system offers an unprecedented resolution down to 2.5 mm and a sensitivity of 415 cps/MBq in scans of human head sized phantoms when a collimator with 3-mm-diameter pinholes is used (Beekman *et al* 2015). These enhanced resolution-sensitivity tradeoffs are facilitated by the systems' design in which all pinholes are focusing on a central volume. This central volume is termed the complete data volume (CDV). For a scan of an object larger than the CDV, the bed is translated in order to extend the volume with ensured sufficient angular sampling. Subsequently, all pinhole projections from all bed positions together are used for image reconstruction of the entire volume using the scanning focus method (Vastenhouw and Beekman 2007).

Recently, we showed that scans of a region which contains a limited number of transaxial slices of the brain (up to 36 mm) can be performed by G-SPECT-I using only 4 bed translations, demanding an estimated overhead time of seconds and thus allowing for very fast dynamic imaging (Chen *et al* 2018). The present paper aims to optimize bed translations of G-SPECT-I for full brain scanning, which is commonly done in brain perfusion studies. To maximize effective sensitivity, scanning speed as well as 4D SPECT frame rate, we investigated (i) confining the axial length to the minimum required, and (ii) limiting the number of bed translations while avoiding truncation artifacts or undersampling, all based on extensive G-SPECT-I simulations including attenuation modeling. Resulting images were assessed both visually and quantitatively.

2. Methods

2.1. System design

The G-SPECT-I scanner (figure 1) consists of nine scintillation gamma detectors each comprised of a $595 \times 472 \times 9.5\,mm^3$ NaI(Tl) crystal based cameras, an interchangeable collimator, a precisely controlled *xyz*-stage for bed translation, three optical cameras and an appropriate user interface for the selection of the scanning volume of interest (VOI) based on the optical cameras (Beekman 2011, Branderhorst *et al* 2011). The collimator assumed in this paper for brain imaging has a total of 54 pinholes (Beekman *et al* 2015). All pinholes are focusing towards the collimator's center, offering a CDV with a transaxial diameter and axial length of 100 mm and 60 mm, respectively. Note that for activity in the large volume of the gantry outside the CDV, the emitted photons are still captured by a part of the pinholes (see figure 1). Other details concerning the G-SPECT-I system have been explained in Chen *et al* (2018).

2.2. Simulation set up

A digital Zubal phantom (Zubal *et al* 1994) was used for simulating normal brain perfusion images (figure 2). The activity map was generated by segmenting the Zubal phantom into grey matter, white matter and cerebral spinal fluid (CSF) and assigning activity concentrations to these regions with a ratio of 4:1:0, respectively, as in Glick and Soares (1997), Stodilka *et al* (2000) and Pato *et al* (2015). We forced the phantom to be perfectly symmetric by mirroring the phantom left hemisphere to the right. This was to avoid any bias induced by the intrinsic left–right asymmetry of the Zubal phantom during image analysis. This phantom was subsequently interpolated (trilinearly) in PMOD v4.0 (PMOD Technologies Ltd, Switzerland) from its original size of $1.1 \times 1.1 \times 1.4\,mm^3$ to $0.75\,mm^3$ voxel size, half the voxel size of the reconstructed image ($1.5\,mm^3$), to mimic a continuous activity distribution reconstructed on a discrete grid. System matrices for forward projection of the activity distribution and reconstruction were both generated using a set of ^{99m}Tc (140 keV) point source measurements and geometrical modeling (van der Have *et al* 2008). To obtain realistic simulated projections, effects of attenuation were included using a voxelized ray tracer (Goorden *et al* 2016, Wang *et al* 2017). Attenuation map were obtained by assigning regions in the Zubal phantom to bone, soft tissue and air with an attenuation coefficient of 0.31,

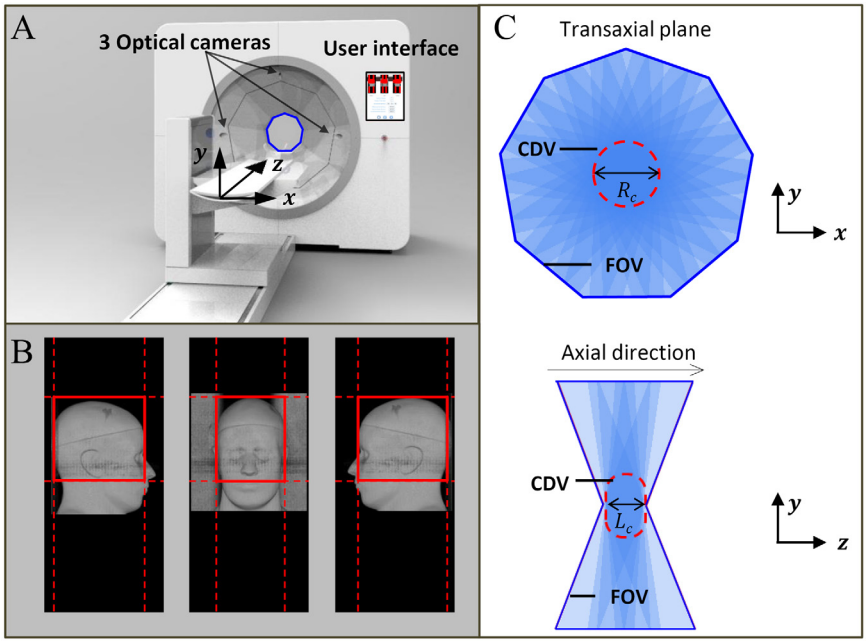

Figure 1. Illustration of the G-SPECT-I scanner. (A) G-SPECT-I system with three optical cameras and a user interface for VOI selection; (B) an example of how VOI selection is done with the user interface. The user interface takes the images from three optical cameras as input. (C) The CDV in transaxial view (top image) and along axial direction (bottom image). The CDV is the volume 'seen' by all pinholes; it has a transaxial diameter R_c of 100 mm and an axial length L_c of 60 mm. The entire field of view (FOV) of the scanner, at one bed position, is much larger than the CDV; it extends over the gantry as shown in the figure.

0.15 and 0 cm^{-1}, respectively (figure 2(C)). Although attenuation was included in simulating projections, no attenuation correction was performed on the reconstructed images. Similarity regulated OSEM (Vaissier *et al* 2016) with eight subsets and ten iterations was performed using the scanning focus method (Vastenhouw and Beekman 2007) to combine all projections from all bed positions simultaneously into image reconstruction.

2.3. Noise-free simulations for bed sequence optimization

Bed sequence optimization was performed using noise-free simulations to quantify errors solely induced by sampling. Sequences investigated here all follow a multi-planar trajectory, meaning that bed positions in each transaxial plane are replicated along axial direction to extend the scan length. To serve as a reference, we first simulated an oversampled full brain scan obtained by (i) scanning the full axial length of the brain; (ii) keeping a small separation (compared to the 60 mm length of the CDV) of 21 mm between consecutive axial positions; and (iii) using a large number of 16 bed positions in each transaxial plane. This reference scan thus employs a total number of 128 small bed translations (eight axial and 16 transaxial positions).

Subsequently, to optimize the bed translation path, a series of scans using a reduced number of bed positions were simulated and compared to the reference scan. This optimization was done according to the following three steps (see also figure 3).

(1) Confine the axial scan length by searching the maximum allowed edge margin D_{em} that still allows for artifact-free whole brain imaging.
(2) Maximize the separation D_{sp} between consecutive axial positions to facilitate a minimum number of axial positions.
(3) Further minimize the required number of transaxial positions per plane N_{tr}, using the optimal settings found in the previous steps.

Each step is explained in detail in the subsections below.

2.3.1. *Axial edge margin D_{em}*

To find the maximum 'safe' edge margin D_{em}, we gradually increased D_{em} from 0 mm (reference scan) to 10.5 mm, 21 mm, 31.5 mm, 42 mm, 52.5 mm (as shown in figure 3(A) which illustrates the two extreme cases). Oversampling in the region between the first and last sampling plane was always ensured by using a small D_{sp} of 21 mm and 16 bed positions in the transaxial plane, the same settings as used for the reference scan.

2.3.2. Axial separation between consecutive positions D_{sp}

The optimal axial separation was investigated by gradually increasing the value of D_{sp} from 21 mm up to 60 mm (the length of the CDV). To have a fair comparison among scans with different D_{sp}, a target slice was adopted, around which axial positions were placed symmetrically (see figure 3(B)). Here the value of D_{sp} was set to be 21 mm, 30 mm, 39 mm, 48 mm and 57 mm (increasing at a multiple of 2×1.5 mm for the symmetric placement).The target slice was placed at the center of the thalamus, which contains rich perfusion patterns and involves multiple important subcortical structures (e.g. caudate, putamen). We regard this slice to be the most 'problematic' for all sequences since it locates exactly in between two sampling planes in all cases. Meanwhile, for all scans with different axial separations it was ensured that the axial length was sufficiently long. In principle, this could be accomplished by placing the first/last axial position at a common top/bottom edge margin (e.g. all at the 'safe edge' found in the previous step) and adding axial positions in between. However, this greatly limits the choice for D_{sp}. Therefore, in this study axial bed positions with a designated separation were added until *at least* the 'safe' edge margin (figure 3(B)).

2.3.3. Transaxial positions N_{tr}

The findings in the aforementioned axial placement step were used as a starting point to further optimize sequence design in the transaxial plane. We kept D_{em} at the maximum 'safe' edge margin while making sure that D_{sp} was not larger than the 'safe' axial separation (see figure 3(C)) and we gradually decreased the number of transaxial positions. The design of all transaxial bed sequences was based on the previously proposed protocol described in Chen *et al* (2018), which assumes that a VOI is selected in the transaxial plane based on the subject's head contour which could be done using the G-SPECT-I user interface (figure 1(B)). A sequence was then designed based on the selected VOI and a transaxial data-completeness model which ensures sampling sufficiency in the convex hull surrounding the CDVs (Chen *et al* 2018). An illustration of the designed transaxial sequences for a G-SPECT-I brain perfusion scan based on this protocol is displayed in figure 3(C); from an oversampled sequence using 16 bed positions per transaxial plane, to sequences using 8, 6 and 4 bed positions per plane.

2.4. Noisy simulations

To place the sampling-induced deviations in the context of image variations due to statistical uncertainty caused by the limited number of detected photons, we additionally performed reconstructions with noisy projection data (for 20 Poisson noise realizations based on the noiseless projections). This was done for the reference sequence as well as for a selected number of sequences with reduced number of bed positions. These noisy simulations assumed a total of 50 MBq of ^{99m}Tc in the brain (Van Laere *et al* 2000, Nobili *et al* 2002, Bowen *et al* 2011) and were representative for a scan time of 30 min.

2.5. Evaluation

Assessment of the simulated perfusion scans was performed by visual inspection and quantitative ROI analysis. The latter was achieved by calculating the BUR and the asymmetry index (AI) in selected ROIs. These two metrics are given by

$$\mathrm{BUR} = \frac{C_{target}}{C_{background}} \tag{1}$$

$$\mathrm{AI} = \frac{C_{R-target} - C_{L-target}}{C_{R-target} + C_{L-target}} \times 200\%. \tag{2}$$

Here C_{target} and $C_{background}$ denote the mean uptake value in the target and background ROI, respectively. In this work the entire cerebellum (figure 4(F)) directly segmented from the Zubal phantom was used as the background region. The mean uptake value $C_{R-target}$ is the measurement from the ROI in the right hemisphere while $C_{L-target}$ is that of the corresponding ROI in the left hemisphere.

Varied ways of target ROI definition are used for perfusion SPECT assessment across studies. One of the common approaches entails manually delineating ROIs in the four big lobes (i.e. frontal, temporal, parietal and occipital lobe), sub-regions of the lobes (e.g. inferior and superior frontal lobe, lateral and medial temporal lobe, etc), and/or in subcortical structures (e.g. cingulate, thalamus, etc) (Charpentier *et al* 2000, Tsolaki *et al* 2001, Staffen *et al* 2006, McNeill *et al* 2007, Colloby *et al* 2010). Besides, automated methods -which could reduce labor and variability compared to manual ROI placements- are often performed by registering subject scans to a template (e.g. an averaged scan from databases) or an atlas (e.g. Talairach atlas). However, this generally requires subject MR scans, templates with already segmented ROIs, etc, while displacement due to misregistration, possibly a few mm (Grova *et al* 2001, Radau *et al* 2001), could bring bias/errors for quantification on the simulated high resolution images. In addition, some studies implement 'polar maps' to generate ROIs by simple image processing on subject SPECT scans. The polar map delineates regions along the periphery of the brain in the transaxial

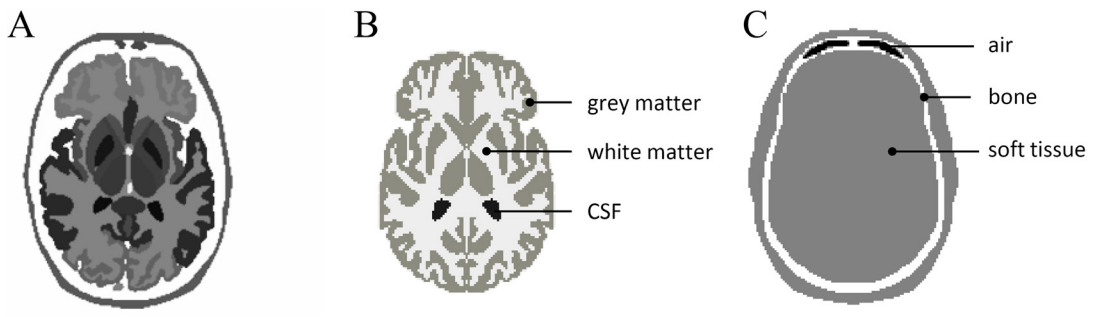

Figure 2. Phantoms used for brain perfusion simulation: (A) the Zubal phantom, (B) activity distribution in phantom, and (C) attenuation map. Tracer concentration in grey matter, white matter and CSF is set to be 4:1:0. Attenuation coefficients assigned to bone, soft tissue and air are 0.31, 0.15 and 0 cm^{-1}, respectively.

plane covering most of the grey matter, where manually drawn ROIs are often placed. The latter approach of ROI definition was implemented in our work. Meanwhile, we also incorporated some ROIs from subcortical structures and in the coronal plane to make the measurement more comprehensive as they have also been used in literature (Tsolaki *et al* 2001, Colloby *et al* 2010).

A total number of 51 target ROIs was used (see figure 4), among which 36 ROIs were placed in three transaxial planes, 9 ROIs in two coronal planes and 6 subcortical ROIs (caudate, putamen and thalamus in both hemispheres) were directly segmented from the 3D Zubal phantom. For the transaxial slices, an inferior (figure 4(A)) and a superior (figure 4(C)) slice were placed at the center of the thalamus and tangential to the cingulate, respectively, as in Cutolo *et al* (2000) and Chiu *et al* (2001). A middle slice (figure 4(B)) was chosen to be the slice exactly in between the two. To generate the polar map regions on the transaxial slice, an annulus region was obtained by segmenting the brain outer boundary from the digital phantom and extending it from the outer boundary inwards for 15 mm, as in Mountz *et al* (1995) and Deutsch *et al* (1997). This annulus was subsequently divided into 12 equal angular sectors. For ROIs in the coronal plane, the orbital and dorsolateral part of the frontal lobe and cingulate (figure 4(D)), as well as the mesial and lateral part of the temporal lobe (figure 4(E)) were considered, as in Chiu *et al* (2001). These transaxial and coronal ROIs have a size in the range of 0.4–1.0 cm^3 with a mean value of 0.8 cm^3. The subcortical ROIs (as displayed in figure 4(A) on one transaxial slice) vary in size from 4.4–5.7 cm^3. Figure 4(F) illustrates the location of the selected transaxial and coronal planes as well as the cerebellum in the brain.

For each simulated scan, its BUR and AI values in all 51 ROIs were calculated and compared to those from the (noise-free) reference scan. We assessed the magnitude of the deviations from this reference scan when scanning with various bed sequences. These deviations are defined as:

$$\text{Dev BUR} = \frac{|\text{BUR} - \text{BUR}_{\text{ref}}|}{\text{BUR}_{\text{ref}}} \times 100\% \tag{3}$$

$$\text{Dev AI} = |\text{AI} - \text{AI}_{\text{ref}}|\,. \tag{4}$$

Here Dev stand for the deviation from the reference scan, while BUR_{ref} and AI_{ref} are the BUR and AI values of the reference. The deviation of AI is calculated directly by subtracting the AI_{ref}, since AI is already a normalized index expressed in percentage. Note that the BURs are always positive (equation (1)) and AIs here could be either positive or negative (equation (2)).

For all images presented in this paper, the noise-free scans were post filtered with a 3D Gaussian filter of 4 mm full width at half maximum (FWHM) and displayed with a slice thickness of 1.5 mm. The noisy scans were 6 mm-FWHM Gaussian filtered and displayed with a larger slice thickness of 6 mm to suppress small local fluctuations due to noise. For quantitative analysis of all scans, measurements were performed on the unfiltered images to avoid any bias from filtering. Additionally, we included some quantitative results obtained from 6-mm-FWHM Gaussian filtered images for a selected number of scans, since quantification of clinical SPECT is commonly performed on filtered images.

3. Results

3.1. Noise-free simulations

3.1.1. Axial edge margin D_{em}

Figure 5(A) shows the sagittal view of simulated perfusion images with an increasing edge margin D_{em}. The red lines indicate the locations of the first/last axial bed positions while the dotted white lines denote

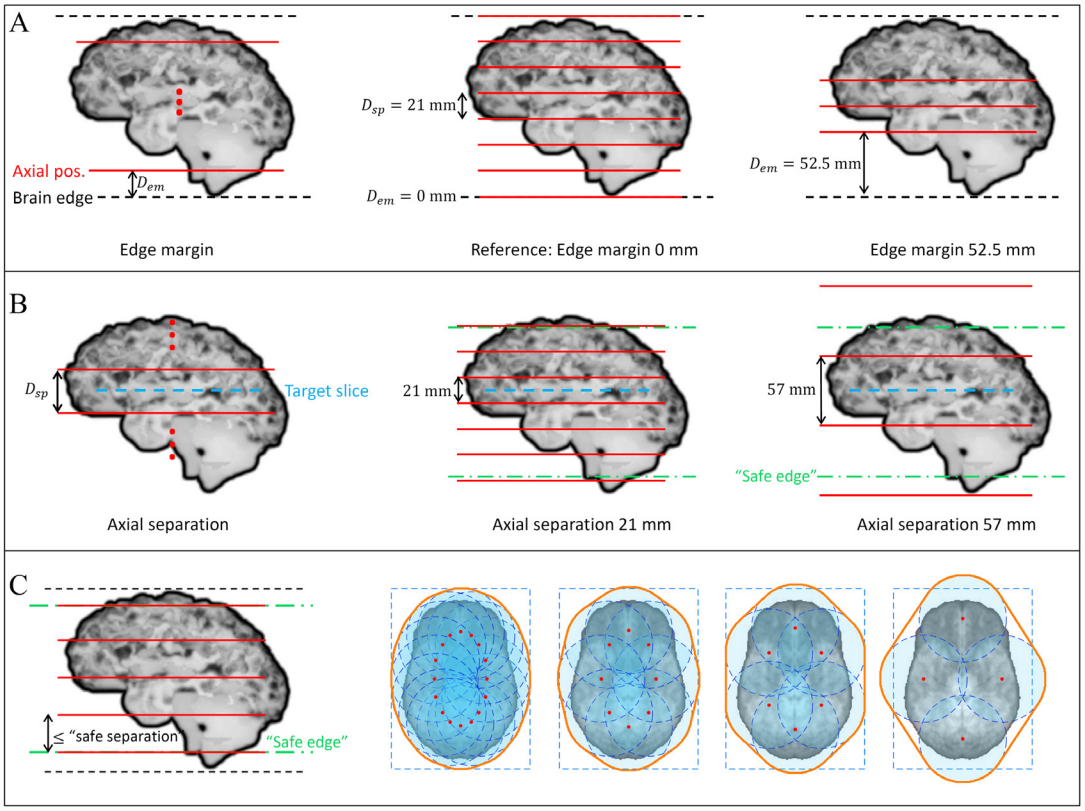

Figure 3. Illustration of the bed sequence optimization for (A) edge margin D_{em}, (B) axial separation D_{sp}, and (C) number of transaxial bed positions N_{tr}. The brain image shown represents a maximum intensity projection of the brain perfusion phantom in the coronal view. In (A), oversampling in the brain between the first and last sampling planes is always ensured by using a safe D_{sp} of 21 mm and a N_{tr} of 16. In (B), bed positions are added until at least the 'safe' edge found in step (A). In (C) the left figure illustrates the final axial position placement, based on the results of the optimal D_{em} and D_{sp}. With this axial placement, sampling sequences with a N_{tr} of 16, 8, 6 and 4 are tested which are displayed at the right. The red dots highlight the transaxial bed positions, and the blue circles indicate the outer contours of the CDVs. The dashed blue box denotes the selected VOI on the transaxial plane. The convex hull of the CDVs, in which complete data is obtained, is represented by the orange line.

the upper/bottom edge of the brain. Compared to the reference scan (with $D_{em} = 0$ mm), scans with a D_{em} up to 31.5 mm appear hardly degraded upon visual inspection while further increasing D_{em} to 42 mm or 52.5 mm results in some artefacts at the edges of the brain. For an additional check, a top and a bottom transaxial slice are selected and displayed in figure 5(B). Image profiles on these two transaxial slices are displayed in figure 5(C). Figures 5(B) and (C) confirm the sufficient coverage of the brain for scans with a maximum D_{em} of 31.5 mm as structures in the top or bottom transaxial slices are well preserved compared to the reference scan.

3.1.2. Axial separation D_{sp} between consecutive sampling planes

To compare the scans with different D_{sp}, the target slice (which always locates exactly in between two sampling planes) as well as image profiles are shown in figures 6(A) and (B), respectively for all sequences. Figure 6 shows that visual differences between the simulated images acquired with varied values of D_{sp} are small; patterns are well preserved with no obvious distortions even for a value of D_{sp} of 57 mm. This is further confirmed by the coronal view comparison in figure A1 in the appendix.

To quantitatively assess the effect of increasing D_{sp}, we calculated brain uptake ratio BUR for the 12 polar map regions on the target slice (figure 7(A)). Compared to the reference image, scanning with an increased value of D_{sp} up to 57 mm achieves comparable BUR measurements (maximal deviation of 6.0% from the reference) among all selected ROIs on the target slice.

Besides a direct comparison of the BURs on the target slice, deviations from the reference scan among all 51 ROIs in the entire brain are calculated and displayed in figure 7(B). Due to the large number of ROIs assessed, only the maximum and mean deviation from all ROIs are plotted. Figure 7(B) demonstrates that deviations from the reference for the tested scans acquired with different D_{sp} are all below 7%. For the scan with a D_{sp} of 48 mm, the BUR and AI deviate maximally 5.0% and 3.2%, respectively, while the mean deviations read only 1.3% and 0.8%. Based on these visual and quantitative results (figures 6–7), a maximum axial separation D_{sp} of 48 mm is used for further transaxial sequence optimization.

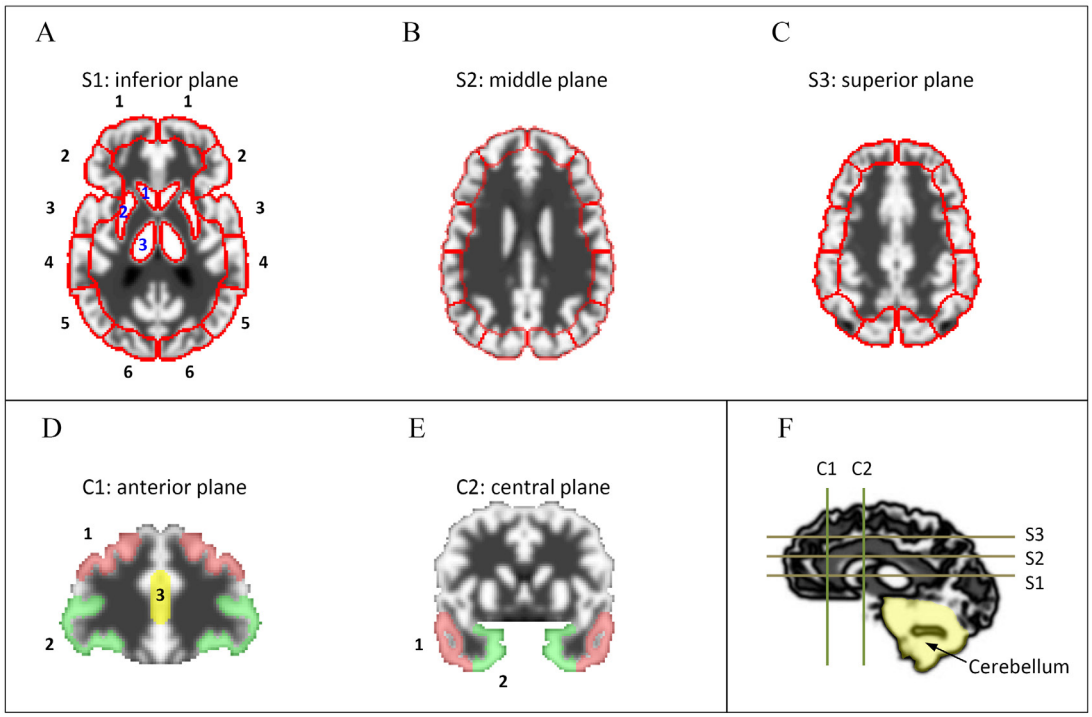

Figure 4. Illustration of the 51 target ROIs for quantitative analysis. Panels (A)–(C) show ROIs in three transaxial slices. Panels (D) and (E) display the ROIs in two coronal slices. Panel F indicates the location of the selected transaxial or coronal slices in the brain. In each transaxial slice, 12 peripheral ROIs are segmented symmetrically on the left and right hemisphere. The subcortical regions in the inferior plane are depicted in panel (A).

3.1.3. Transaxial sampling sequence

Figure 8 shows a comparison of scans with different numbers of transaxial bed positions N_{tr}. All scans (except the oversampled reference) use the same axial bed position placement (figure 8(A)) based on the previous results (optimal D_{em} and D_{sp}) and adjusted to the size of Zubal phantom; we keep D_{em} to be 31.5 mm while adding axial positions such that D_{sp} is not larger than 48 mm (42 mm here). Figure 8(A) shows two transaxial slices which are both in between two sampling planes, while figure 8(B) gives a comprehensive comparison of the transaxial images from the top to the bottom of the brain. Additionally, as other views are also important for perfusion scan assessment, we include more image comparisons for the coronal view in the appendix (figure A2). Both the transaxial and coronal view results show that reducing the number of bed positions from the oversampled reference scan to 18 (3 axial positions combined with 6 transaxial positions) hardly has a visual effect on perfusion images. Further decreasing the number of transaxial bed positions to 4 leads to relatively larger deviations from the reference as well as a slightly degraded left–right symmetry.

A quantitative analysis is included in figure 9 which shows a direct comparison of the BURs for the 12 polar map ROIs on the target slice (figure 9(A)), as well as the maximum and average deviations in BUR and AI from the reference among all 51 ROIs (figure 9(B)). For all the tested transaxial sequences, these deviations are below 9.8%. When using six transaxial positions with the proposed axial placement, the maximum deviation of the two measurements are 5.7% and 5.4% for BUR and AI, respectively, while the mean deviations read only 2.2% and 1.5%. Further decreasing the number of transaxial positions to 4 leads to a maximum deviation of 8.1% and 9.8% for the BUR and AI, respectively, and a mean deviation of 2.9% and 2.7%, respectively.

3.2. Noisy simulations

Noisy simulations were performed for the reference sequence (Noisy-ref) as well as for two selected sequences based on the results above, i.e. the sequence with 18 (Noisy-18: 3 × 6 positions) and 12 positions (Noisy-12: 3 × 4 positions). Examples of the simulated noisy images are shown in figure 10(A).

Quantitative assessment of the BUR and AI deviations from the (noise-free) reference scan are provided in figure 10(B). This figure shows that deviations due to Poisson noise are 3–4 times larger than those induced by sampling; for example, reducing the number of bed positions to 18 or 12 positions leads to a mean (BUR or AI) deviation from the reference in the range of only 1.5%–2.9% when assessed on unfiltered images, while these two mean deviations (BUR and AI) for Noisy-ref are 6.5% and 8.6%, respectively. Using a post filter (6-mm-FWHM Gaussian) either on noise-free or noisy scans could reduce the quantification error typically by a factor of 1.5–2. For example, the sampling induced BUR or AI deviations (with 18 or 12 positions) decrease to mean values of

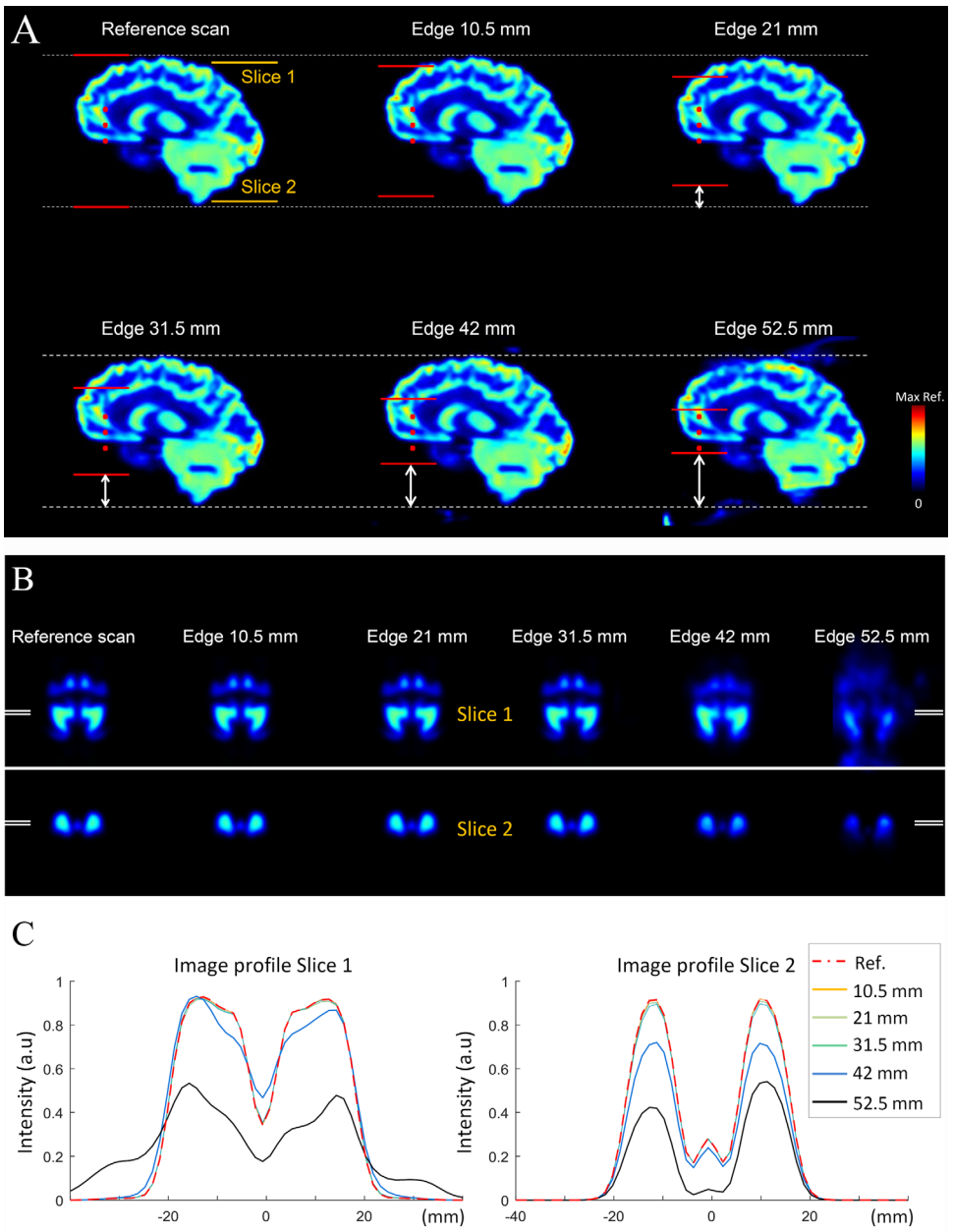

Figure 5. Comparison of scans with different edge margin D_{em}. (A) Simulated sagittal image slices are displayed. The red lines indicate the locations of the first/last axial bed positions and the dotted white lines denote the upper/bottom edge of the brain. The same colormap ranging from 0 to the maximum intensity of the reference scan is used for all simulated perfusion images in this paper. (B) A top and bottom transaxial slice are displayed. The locations of these two slices are indicated in panel (A). Image profiles through each transaxial slice are included and shown in panel (C). These profiles are taken from a line with a width and thickness of 4.5 mm.

0.7%–1.9% when images are filtered, while for the Noisy-ref scans the mean deviation decreases to 4.2% and 2.5% for BUR and AI, respectively.

Compared to Noisy-ref, Noisy-18 achieves a slightly better performance, which could be explained by the increased count yield (1.2 times higher for the more focused 18-position sequence than for the reference sequence). Noisy-12 obtains a similar quantitative accuracy as Noisy-ref for unfiltered images, but slightly larger deviations (0.7% and 0.6% larger mean deviations for BUR and AI, respectively) when assessed on the filtered scans.

4. Discussion

A big challenge in clinical brain imaging is to achieve an excellent resolution-sensitivity tradeoff that allows for visualization of small lesions at a reasonable radiation dose, while fast (dynamic) capabilities that can be used in motion correction are advantageous as well. Previously we have demonstrated excellent resolution-sensitivity tradeoff of the G-SPECT-I scanner in physical phantom scans (Beekman *et al* 2015). The current work presents

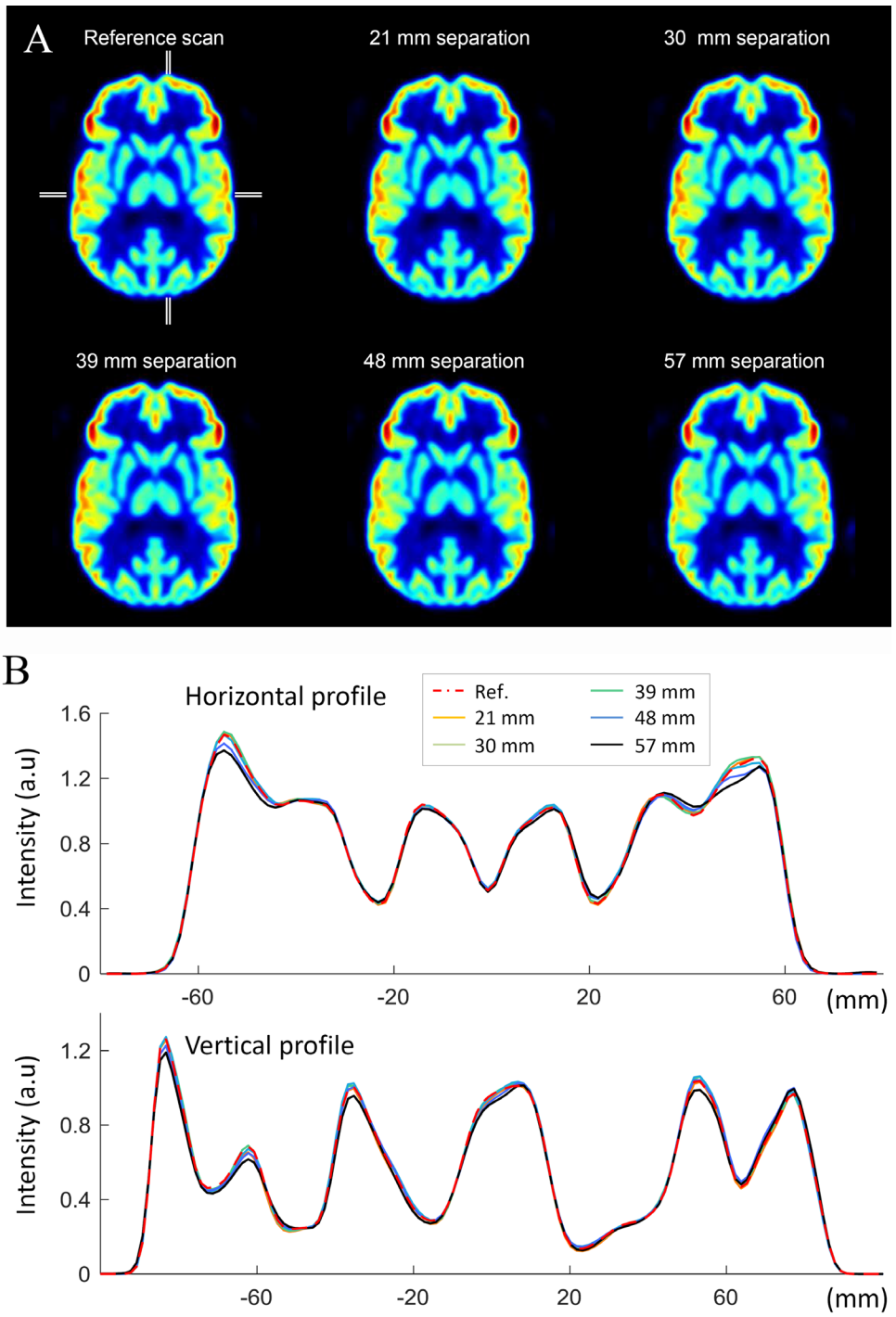

Figure 6. Comparison of the target slice for scans with different axial separations. (A) The target slice is displayed for different scan sequences. (B) A horizontal and a vertical image profile through the target slice are shown. These profiles are taken from a line with a width and thickness of 4.5 mm. Note that the reference scan is simulated using an axial separation of 21 mm and covers the entire brain using 8 axial positions (see figure 3(A)), while the middle image on the first row of panel A (21 mm separation) is simulated with an axial separation of 21 mm and sufficient axial bed positions (5 in this case) are added to reach the safe edge margin of 31.5 mm.

G-SPECT-I acquisition using a limited number of bed translations that still allows artifact-free high resolution whole brain scanning. We estimated the total overhead time of 18 and 12 positions to be only 30 and 20 s, respectively (based on estimations involving the current G-SPECT-I prototype). This may enable fast dynamic studies and multi-frame scans for motion correction.

Note that with G-SPECT-I, overhead time is introduced by the bed translations required to scan volumes larger than the CDV, while for traditional SPECT overhead time is associated with the need to rotate the heads. For traditional scanners with step-and-shoot mode, 64 or 128 views are generally required for sufficient angular sampling (even for a small scanning volume), which results in more than 20 detector stops even for a triple-head

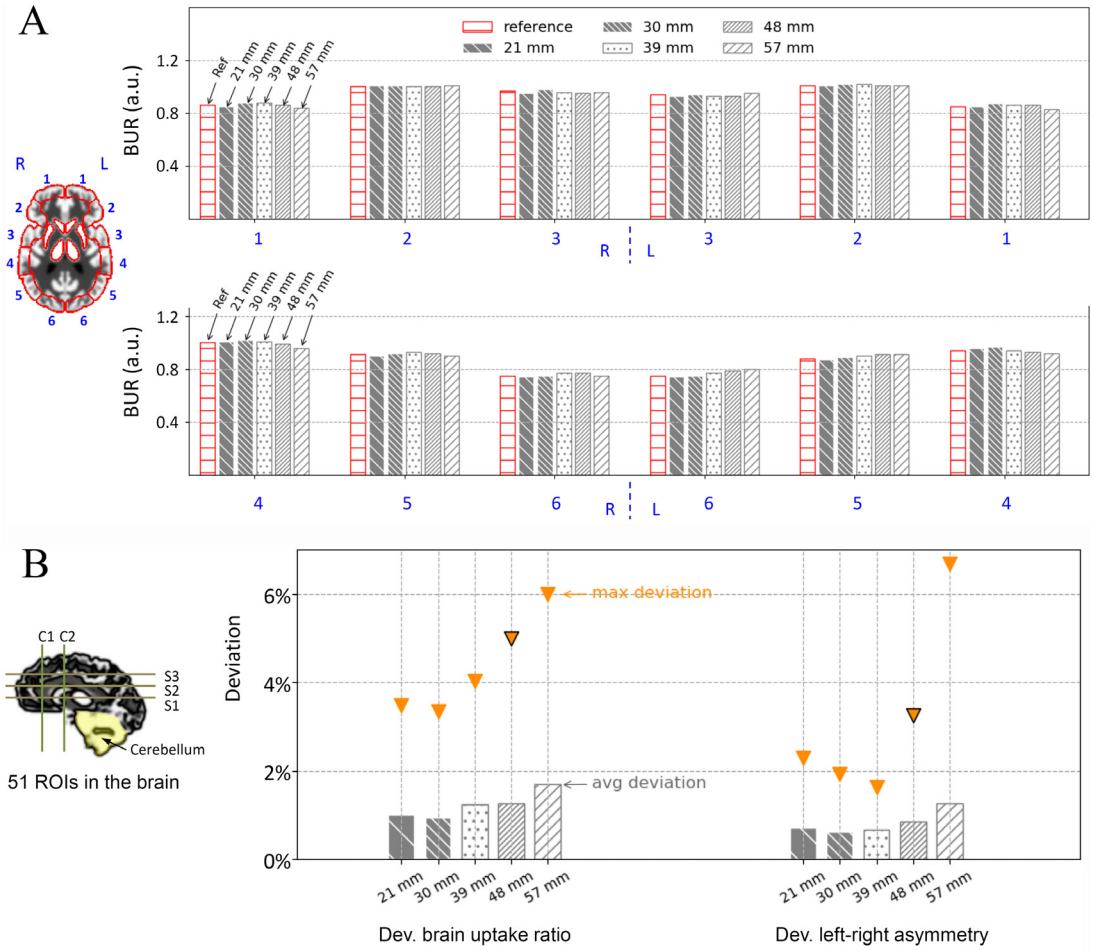

Figure 7. Comparison of the BUR and AI measurements between the reference and scans with an increased axial separation D_{sp}. (A) Direct comparison of the BURs for the tested sequences in ROIs on the target slice; (B) deviations from the reference of the BUR and AI among all 51 ROIs (see figure 4) in the entire brain. The maximum and average deviation are shown with a triangle and a bar, respectively.

system leading to an overhead time of 40–80 s assuming 2–4 s movement time per view, as reported in (Cao *et al* 1996, Mohseni *et al* 2018). Instead, the G- SPECT-I design with stationary detectors offers the flexibility of performing focused scans where only few bed translations are required while also allowing for extended volume scans.

Effects of attenuation were included in the simulation to make results more realistic. No attenuation correction was performed in the reconstruction for multiple reasons. Firstly, we have not yet determined the attenuation correction method (e.g. transmission imaging based, MR based using deep learning, solely SPECT based, etc) to be applied in future G-SPECT-I studies. This is currently under development (Chen *et al* 2019), however further testing and validation is necessary. Besides, there are clinicians do not use it (Modzelewski *et al* 2012), possibly because it can be prone to errors due to small shifts between SPECT and CT (Larsson *et al* 2003, Bateman and Cullom 2005) or because of the limited accuracy of a contour based uniform attenuation. Therefore we felt it was better to prevent mixing of the sampling issues with attenuation correction inaccuracies due to the use of a not fully validated approach for G-SPECT-I at this stage.

In this paper, we firstly performed noise-free simulations to constrain the analysis to sampling problems associated with different sequences, while later noisy simulations were included to investigate the utility of the optimized sequences in realistic noisy situations. The former step demonstrated that reconstructed images were barely affected (both visually and quantitatively) when the number of bed translations was decreased from 128 down to 18; when further decreasing the number of translations to 12, a somewhat larger deterioration from the reference scan (maximum deviation of 9.8%, see figure 9) and some visual deviations (see figure 8) were observed. This maximum deviation with the use of a 12-position sequence decreases to 6.9% when quantifications were done on 6-mm-FWHM Gaussian filtered scans (figure 10(B)). In addition, the noisy simulations showed that in the presence of noise, the deviations due to using 18-position or 12-position sequences are almost negligible (3–4 times smaller) compare to those induced by noise. Note that in the noisy simulations bed movement overhead time was neglected as it highly depends on the number of frames in data acquisition and the bed

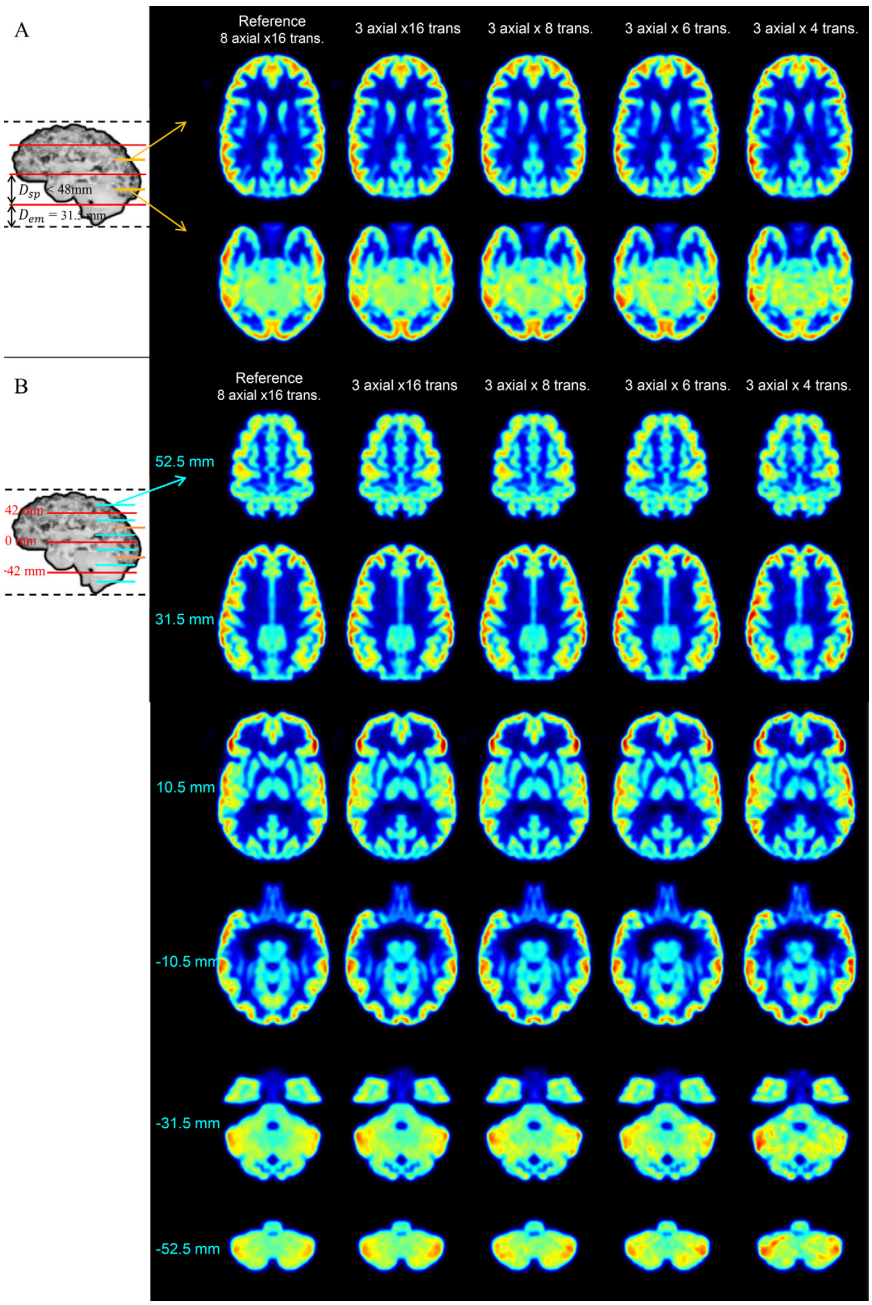

Figure 8. Comparison between the reference scan and scans with different transaxial bed positions. (A) Two transaxial slices which are both exactly in between two sampling planes; (B) transaxial slices from top to the bottom of the brain.

in use. Thus in practical SPECT scans when overhead time is playing a role, especially in multi-frames studies, one would expect a relatively larger benefit when using sequences with 18 and 12 positions than what is provided in figure 10.

For focused scans when only a part of the brain is of interest, the number of bed translations can be further reduced without sacrificing image quality by axially restricting the scan length to just cover the target volume. An example of such an implementation was demonstrated in Chen *et al* (2018) which presented brain dopamine system imaging with only 4 bed translations. Besides, even for whole brain scans which require very high temporal resolutions, as in brain pharmacokinetic studies (Nakano *et al* 1988, Ogasawara *et al* 2001, Komatani *et al* 2004, Gullberg *et al* 2010), utilizing less than 12 positions remains possible, for example by applying an axial separation D_{sp} larger than the currently used value of 48 mm. For such fast scans, the effects of noise would be much more prominent than what was shown in figure 10 such that the compromised accuracy due to sampling may be negligible. This could enable imaging tracers with a very short (biological or physical) half-life, such as ^{133}Xe (biological half-life $\approx$ 40 s), for which scanning with a confined axial length, e.g. 71 mm (Knutsson *et al* 2007) is often already done.

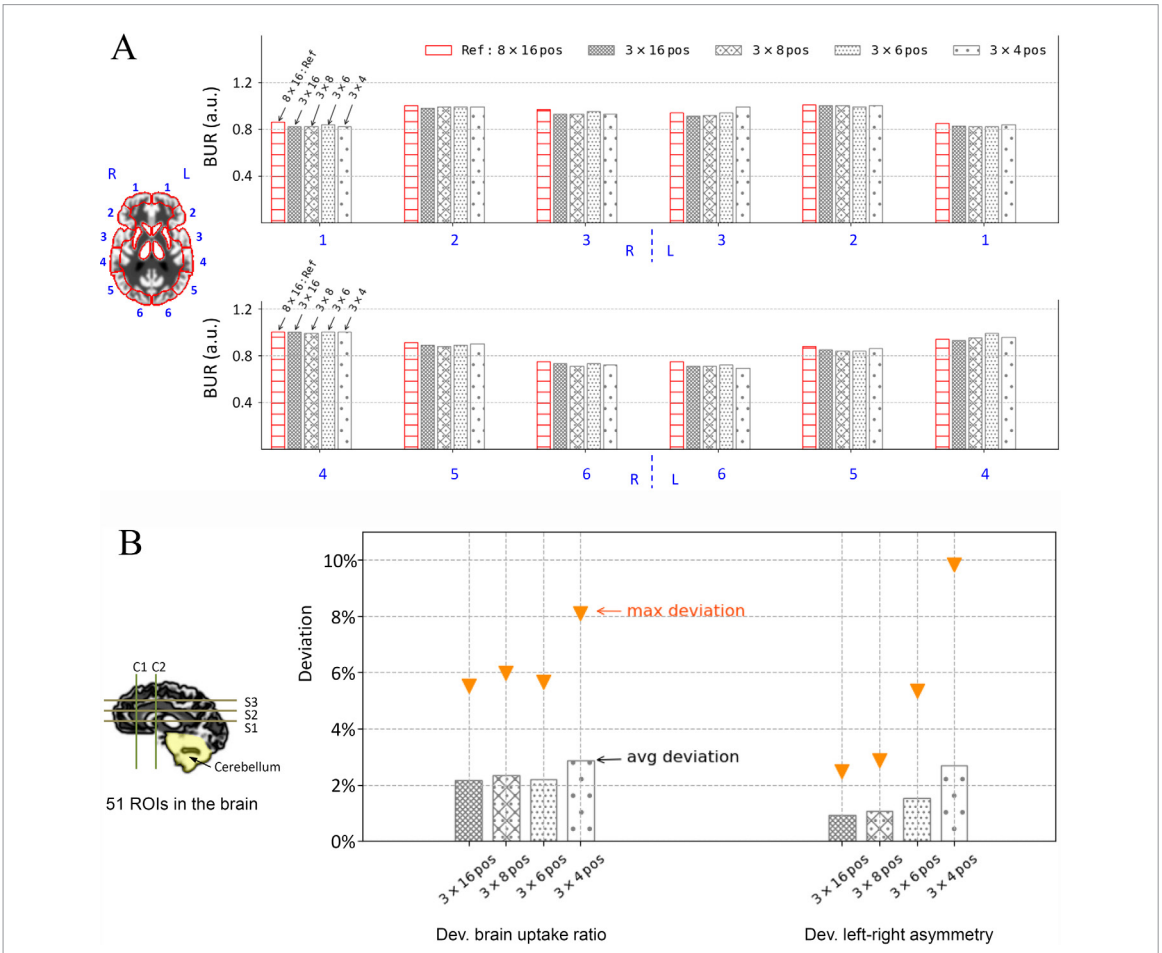

Figure 9. Comparison of the BUR and AI measurements between the reference and several scans each using 3 axial positions but with different numbers of transaxial bed position N_{tr}. (A) Direct comparison of the BURs for the tested sequences in ROIs on the target slice; (B) deviations from the reference of the BUR and AI among all 51 ROIs (see figure 4) in the entire brain. The maximum and mean deviation are shown with a triangle and a bar, respectively.

Aspects which have not yet been studied here could enable even faster dynamic SPECT imaging. We have assumed the same number of transaxial positions at each axial position; in future work one could study using fewer transaxial positions when scanning parts of the brain with smaller dimensions, e.g. the brain's top and bottom. Besides, strategies that enable a continuous bed motion acquisition would be beneficial as in that case counts would constantly be recorded during the entire scan. Such methods have been proposed for PET imaging with bed translations only in axial direction (Dahlbom *et al* 2001, Brasse *et al* 2002, Casey *et al* 2005). For G-SPECT imaging this requires additional investigations. Moreover, collimators that offer a larger CDV are currently under design in our institute. With these developments, one can expect that less or even no bed translations are required, which may help to achieve extremely fast SPECT scans.

5. Conclusion

We have designed and evaluated different bed position sequences for total brain perfusion imaging with a stationary focusing multi-pinhole SPECT system. We found that decreasing the number of bed positions from 128 representing an oversampled scan down to a small number of 18 or 12 positions has minimal effects on image quantification compared to those induced by noise, while the respective overhead times were estimated to be only 30 and 20 s in total. This is important information for developing protocols for fast dynamic brain SPECT and multi-frame scans for motion correction.

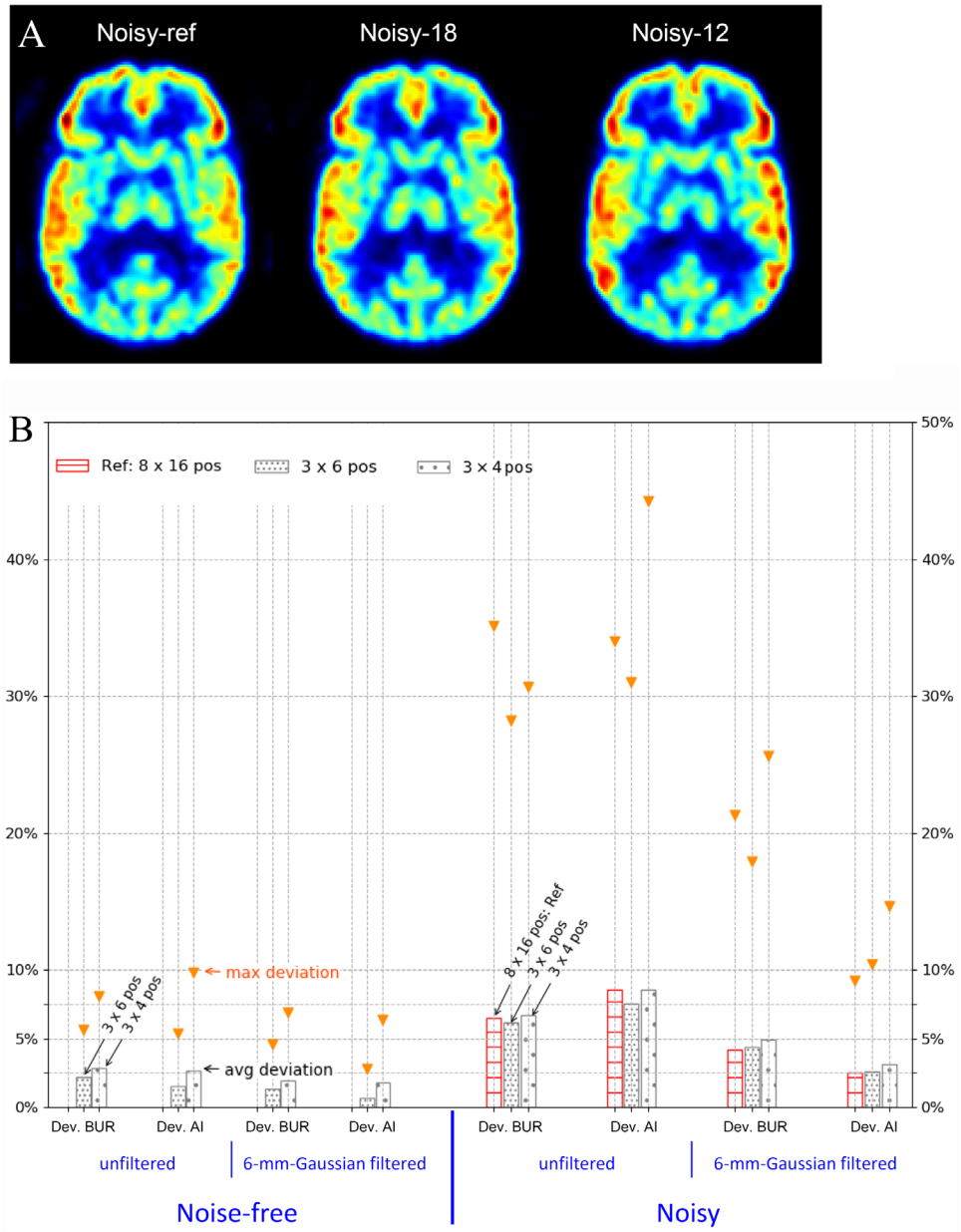

Figure 10. Comparison of the noisy simulations for the reference sequence (Noisy-ref) as well as for sequences with 18 (Noisy-18) and 12 positions (Noisy-12). Example of the simulated noisy scans are shown in panel A. Panel B shows the deviations from the (noise-free) reference scan for the noiseless and noisy unfiltered scans and for these scans applying a Gaussian filter of 6 mm FWHM. The maximum and mean deviation are shown with a triangle and a bar, respectively. For the noisy simulations, the maximum and mean deviations were calculated from 51 ROIs and for all 20 noise realizations.

Acknowledgments

Financial disclosures of authors: FB and BV both are employee & shareholder of MILabs BV. This work is conducted with financial support of the Netherlands Organization for Scientific Research (NWO), Physics Valorization Prize 'Ultra-fast, ultra-sensitive and ultra-high resolution SPECT' co-financed by MILabs B.V.

Appendix

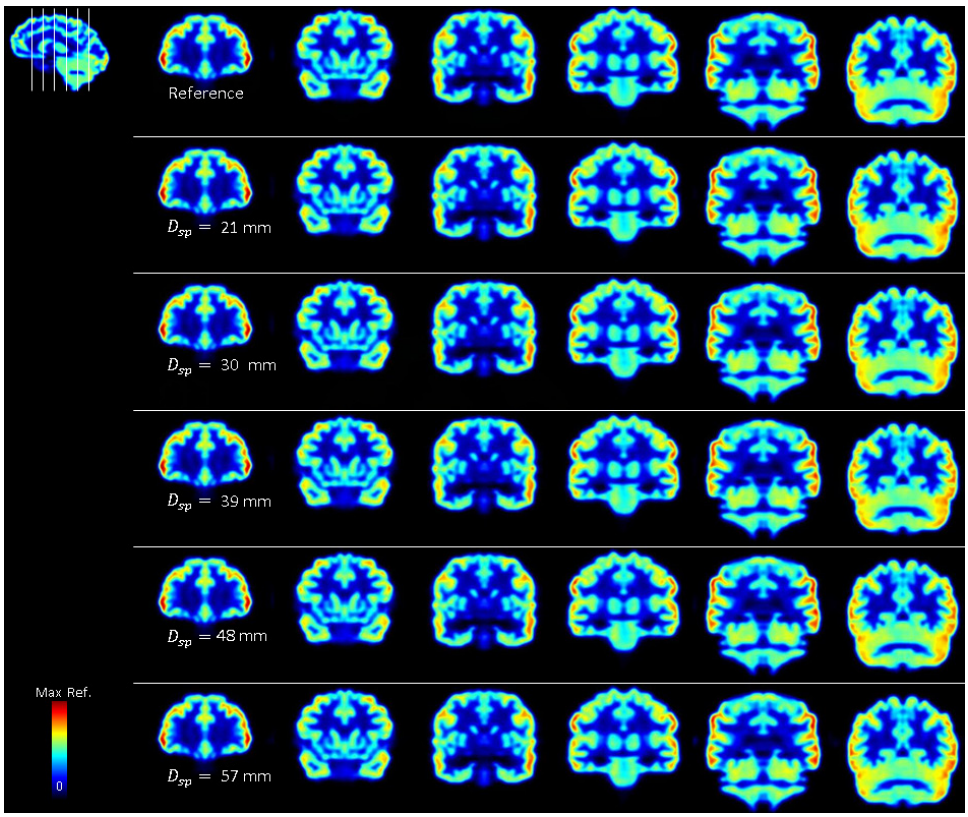

Figure A1. Comparison of simulated perfusion images with the reference image when increasing the axial separation between consecutive sampling planes D_{sp}. Images are shown in the coronal view. Each row corresponds to one simulated scan, with the D_{sp} increasing from 21 mm to 57 mm from the 2nd row to the bottom row. Images from left to right shows the coronal slices from the anterior of the brain to the posterior. The locations of the slices are indicated in the top left image.

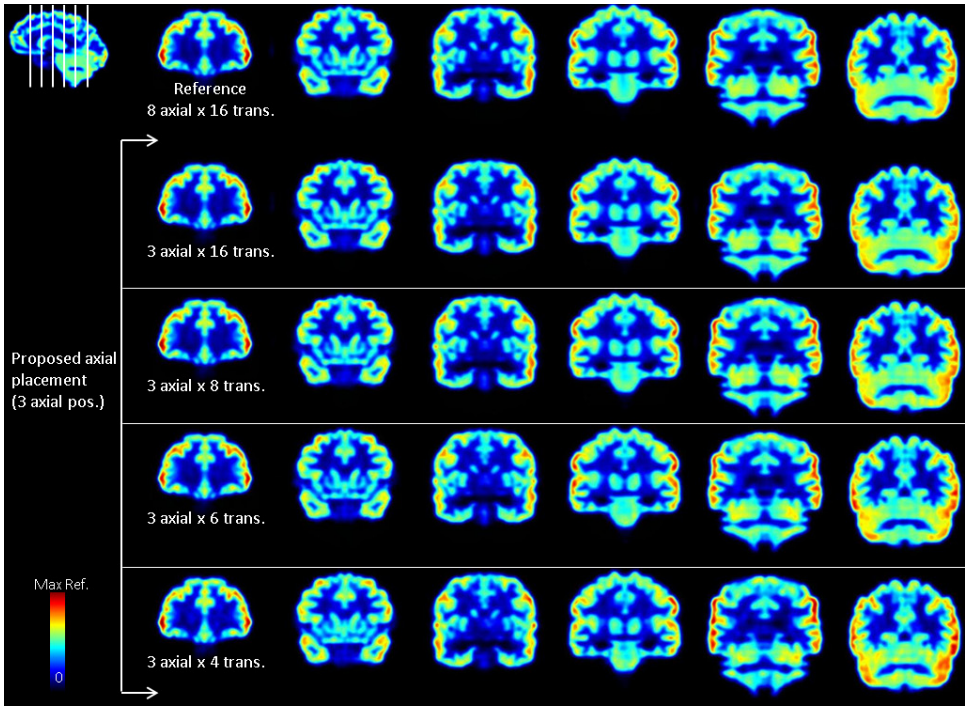

Figure A2. Comparison of simulated perfusion images with the reference image when using the proposed axial position placement but reducing the number of transaxial bed positions N_{tr}. Each row corresponds to one simulated scan, with the N_{tr} decreasing from 16 to 4 positions per plane from the 2nd row to the bottom row. Images from left to right shows the coronal slices from the anterior of the brain to the posterior. The locations of the slices are indicated in the top left image.

References

Amen D G 2015 *Change Your Brain, Change Your Life: Revised and Expanded Edition: The Breakthrough Programme for Conquering Anxiety, Depression, Anger and Obsessiveness* (London: Piatkus Books).

Amen D G, Prunella J R, Fallon J H, Amen B and Hanks C 2009 A comparative analysis of completed suicide using high resolution brain SPECT imaging *J. Neuropsychiatry Clin. Neurosci.* **21** 430–9

Amen D G, Trujillo M, Newberg A, Willeumier K, Tarzwell R, Wu J C and Chaitin B 2011 Brain SPECT imaging in complex psychiatric cases: an evidence-based, underutilized tool *Open Neuroimag. J.* **5** 40–8

Bateman T M and Cullom S J 2005 Attenuation correction single-photon emission computed tomography myocardial perfusion imaging *Semin. Nucl. Med.* **35** 37–51

Beekman F J 2011 Gamma radiation imaging apparatus *US Patent Application No. 13/054,010*

Beekman F J, van der Have F, Goorden M C, Vaissier P E B, van Roosmalen J, During H and Vastenhouw B 2015 G-SPECT-I: a full ring high sensitivity and ultra-fast clinical molecular imaging system with <3 mm resolution *Eur. J. Nucl. Med. Mol. Imaging* **42** S209

Beekman F J, Van der Have F, Vastenhouw B, van der Linden A J, van Rijk P P, Burback J P H and Smidt M P 2005 U-SPECT-I : A novel system for submillimeter-resolution tomography with radiolabeled molecules in mice *J. Nucl. Med.* **46** 1194–200

Befera N, Badea C and Johnson G 2014 Comparison of 4D-microSPECT and microCT for murine cardiac function *Mol. Imaging Biol.* **16** 235–45

Bowen J D, Huang Q, Gullberg G T and Seo Y 2011 Phantom measurements and simulations of cardiac and brain studies using a multipinhole collimator with 20 apertures *IEEE Nuclear Science Symp. Medical Imaging Conf. Records* pp 3417–21

Branderhorst W, Vastenhouw B, Van Der Have F, Blezer E L A, Bleeker W K and Beekman F J 2011 Targeted multi-pinhole SPECT *Eur. J. Nucl. Med. Mol. Imaging* **38** 552–61

Brasse D, Newport D, Carney J P, Yap J T, Reynolds C, Reed J, Bao J, Luk P, Michel C and Townsend D W 2002 Continuous bed motion acquisition on a whole body combined PET/CT system *IEEE Nuclear Science Symp. Conf. Records* vol 2 951–5

Camargo E E 2001 Brain SPECT in neurology and psychiatry *J. Nucl. Med.* **42** 611–23

Cao Z, Maunoury C, Chen C C and Holder L E 1996 Comparison of continuous step-and-shoot versus step-and-shoot acquisition SPECT *J. Nucl. Med.* **37** 2037–9

Casey M E, Luk W K and Reed J H 2005 Continuous tomography bed motion data processing apparatus and method *U.S. Patent* No. 6,915,004

Catafau A M 2001 Brain SPECT in clinical practice. Part I: perfusion *J. Nucl. Med.* **42** 259–71

Charpentier P, Lavenu I, Defebvre L, Duhamel A, Lecouffe P, Pasquier F and Steinling M 2000 Alzheimer's disease and frontotemporal dementia are differentiated by discriminant analysis applied to 99mTc HmPAO SPECT data *J. Neurol. Neurosurg. Psychiatry* **69** 661–3

Chen L, Tsui B M W and Mok G S P 2017 Design and evaluation of two multi-pinhole collimators for brain SPECT *Ann. Nucl. Med.* **31** 636–48

Chen Y, Goorden M C and Beekman F J 2019 Attenuation map estimation from SPECT data only using a convolutional neural network *Poster Session Presented at IEEE Nuclear Science Symp. and Medical Imaging Conf. (Manchester)*

Chen Y, Vastenhouw B, Wu C, Goorden M C and Beekman F J 2018 Optimized image acquisition for dopamine transporter imaging with ultra- high resolution clinical pinhole SPECT *Phys. Med. Biol.* **63** 225002

Chiu N T, Chang Y C, Lee B F, Huang C C and Wang S T 2001 Differences in ^{99m}Tc-HMPAO brain SPET perfusion imaging between Tourette's syndrome and chronic tic disorder in children *Eur. J. Nucl. Med.* **28** 183–90

Colloby S J, Taylor J P, Firbank M J, McKeith I G, Williams E D and O'Brien J T 2010 Covariance 99mTc-exametazime SPECT patterns in Alzheimer's disease and dementia with Lewy bodies: utility in differential diagnosis *J. Geriatr. Psychiatry Neurol.* **23** 54–62

Cutolo M *et al* 2000 Evidence of cerebral hypoperfusion in scleroderma patients *Rheumatology* **39** 1366–73

Dahlbom M, Member S, Reed J and Young J 2001 Implementation of true continuous bed motion in 2D and 3D whole-body PET scanning *IEEE Trans. Nucl. Sci.* **48** 1465–9

Deutsch G, Mountz J M, Katholi C R, Liu H G and Harrell L E 1997 Regional stability of cerebral blood flow measured by repeated technetium-99m-HMPAO SPECT: implications for the study of state-dependent change *J. Nucl. Med.* **38** 6–13

Fakhri G El, Ouyang J, Zimmerman R E, Fischman A J and Kijewski M F 2006 Performance of a novel collimator for high-sensitivity brain SPECT *Med. Phys.* **33** 209–15

Glick S J and Soares E J 1997 Noise characteristics of SPECT iterative reconstruction with a mis-matched projector-backprojector pair *IEEE Trans. Nucl. Sci.* **2** 1518–5

Goorden M C, van der Have F, Kreuger R, Ramakers R M, Vastenhouw B, Burbach J P H, Booij J, Molthoff C F M and Beekman F J 2013 VECTor: A Preclinical Imaging System for Simultaneous Submillimeter SPECT and PET *J. Nucl. Med.* **54** 306–12

Goorden M C, van Roosmalen J, van der Have F and Beekman F J 2016 Optimizing modelling in iterative image reconstruction for preclinical pinhole PET *Phys. Med. Biol.* **61** 3712–33

Grova C, Biraben A, Scarabin J M, Jannin P, Buvat I, Benali H and Gibaud B 2001 A methodology to validate MRI/SPECT registration methods using realistic simulated SPECT data *Int. Conf. on Medical Image Computing and Computer-Assisted Intervention* vol 2208 pp 275–82

Gullberg G T, Reutter B W, Sitek A, Maltz J S and Budinger T F 2010 Dynamic single photon emission computed tomography—basic principles and cardiac applications *Phys. Med. Biol.* **55** R111

Ivashchenko O, van der Have F, Goorden M C, Ramakers R M and Beekman F J 2015 Ultra-high-sensitivity submillimeter mouse SPECT *J. Nucl. Med.* **56** 470–5

Ivashchenko O, van der Have F, Villena J L, Groen H C, Ramakers R M, Weinans H H and Beekman F J 2014 Quarter-millimeter-resolution molecular mouse imaging with U-SPECT + *Mol. Imaging* **14** 7290–2014

Juni J E, Waxman A D, Devous M D, Tikofsky R S, Ichise M, Van Heertum R L, Carretta R F and Chen C C 2009 Procedure guideline for brain perfusion SPECT using ^{99m}Tc radiopharmaceuticals 3.0 *J. Nucl. Med. Technol.* **37** 191–5

Kim S and Mountz J M 2011 SPECT imaging of epilepsy: an overview and comparison with F-18 FDG PET *Int. J. Mol. Imaging* **2011** 1–9

King M A, Zubal I G, Mukherjee J M, Könik A, Dey J and Licho R 2012 Design of a multi-pinhole collimator for I-123 DaTscan imaging on dual-headed SPECT systems in combination with a fan-beam collimator *IEEE NSS/MIC 2012* pp 3170–3

Knowlton R C 2006 The role of FDG-PET, ictal SPECT, and MEG in the epilepsy surgery evaluation *Epilepsy Behav.* **8** 91–101

Knutsson L, Bo S, Larsson E, Risberg J, Gustafson L, Passant U, Ståhlberg F and Wirestam R 2007 Absolute quantification of cerebral blood flow in normal volunteers : correlation between Xe-133 SPECT and dynamic susceptibility contrast MRI *J. Magn. Reson. Imaging* **920** 913–20

Komatani A, Sugai Y and Hosoya T 2004 Development of 'super rapid dynamic SPECT,' and analysis of retention process of ^{99m}Tc-ECD in ischemic lesions: comparative study with 133Xe SPECT *Ann. Nucl. Med.* **18** 489–94

Larsson A, Johansson L, Sundstro T and Åhlström K 2003 A method for attenuation and scatter correction of brain SPECT based on computed tomography images *Nucl. Med. Commun.* **24** 411–20

Lee T-C, Ellin J R, Huang Q, Shrestha U, Gullberg G T and Seo Y 2014 Multipinhole collimator with 20 apertures for a brain SPECT application *Med. Phys.* **41** 112501–7

McNeill R, Sare G M, Manoharan M, Testa H J, Mann D M A, Neary D, Snowden J S and Varma A R 2007 Accuracy of single-photon emission computed tomography in differentiating frontotemporal dementia from Alzheimer's disease *J. Neurol. Neurosurg. Psychiatry* **78** 350–5

Modzelewski R, Janvresse E, de la Rue T and Vera P 2012 Comparison of heterogeneity quantification algorithms for brain SPECT perfusion images *EJNMMI Res.* **2** 1–10

Mohseni M, Faghihi R, Haghighatafshar M and Entezarmahdi S M 2018 Effects of the attenuation correction and reconstruction method parameters on conventional cardiac dynamic SPECT *Medicine* **97** e12239

Mountz J M, Bradley L A, Modell J G, Alexander R W, Triana A M, Aaron L A, Stewart K E, Alarcon G S and Mountz J D 1995 Fibromyalgia in women *Arthritis Rheum.* **38** 926–38

Mukherjee J M, Dey J and King M A 2014 Image reconstruction methods for I-123 DaTscan imaging using a multi-pinhole and fan collimator dual-headed SPECT system *2014 IEEE Nuclear Science Symp. and Medical Imaging Conf.* pp 1–3

Nakano S, Kinoshita K, Jinnouchi S, Hoshi H and Watanabe K 1988 Dynamic SPECT with Iodine-123 IMP in Meningiomas *J. Nucl. Med.* **29** 1627–32

Nobili F, Koulibaly M, Vitali P, Migneco O, Mariani G, Ebmeier K, Alberto P, Robert P, Rodriguez G and Darcourt J 2002 Brain perfusion follow-up in Alzheimer's patients during treatment with acetylcholinesterase inhibitors *J. Nucl. Med.* **43** 983–91

Ogasawara K, Ogawa A, Ezura M, Konno H, Doi M, Kuroda K and Yoshimoto T 2001 Dynamic and static ^{99m}Tc-ECD SPECT imaging of subacute cerebral infarction: comparison with 133Xe SPECT *J. Nucl. Med.* **42** 543–7

Pato L R V, Vandenberghe S, Zedda T and Van Holen R 2015 Parallel-hole collimator concept for stationary SPECT imaging *Phys. Med. Biol.* **60** 8791–807

Radau P E, Slomka P J, Julin P, Svensson L and Wahlund L O 2001 Evaluation of linear registration algorithms for brain SPECT and the errors due to hypoperfusion lesions *Med. Phys.* **28** 1660–8

Santra A and Kumar R 2014 Brain perfusion single photon emission computed tomography in major psychiatric disorders: from basics to clinical practice *IJNM Off. J. Soc. Nucl. Med. India* **29** 210–21

Sensakovic W F, Hough M C and Kimbley E A 2014 ACR testing of a dedicated head SPECT unit *J. Appl. Clin. Med. Phys.* **15** 372–81

Staffen W, Schönauer U, Zauner H, Spindler I, Mair A, Iglseder B, Bernroider G and Ladurner G 2006 Brain perfusion SPECT in patients with mild cognitive impairment and Alzheimer's disease: comparison of a semiquantitative and a visual evaluation *J. Neural Transm.* **113** 195–203

Stam M K, Verwer E E, Booij J, Adriaanse S M, de Bruin C M and de Wit T C 2018 Performance evaluation of a novel brain- dedicated SPECT system *EJNMMI Phys.* **5** 1–14

Stoddart H A and Stoddart H F 1992 New multi-dimensional reconstructions for the lZdetector, scanned focal point, single-photon tomograph *Phys. Med. Biol.* **37** 579–86

Stodilka R Z, Kemp B J, Prato F S, Kertesz A, Kuhl D and Nicholson R L 2000 Scatter and attenuation correction for brain SPECT using attenuation distributions inferred from a head atlas *J. Nucl. Med.* **41** 1569–78

Tsolaki M, Sakka V, Gerasimou G, Dimacopoulos N, Chatzizisi O, Fountoulakis K N, Kyriazis G, Papanastasiou J and Kazis A 2001 Correlation of rCBF (SPECT), CSF tau, and congnitive function in patients with dementia of the Alzheimer's type, other types of dementia, and congrol subjects *Am. J. Alzheimers. Dis. Other Demen.* **16** 21–31

Vaissier P E B, Beekman F J and Goorden M C 2016 Similarity-regulation of OS-EM for accelerated SPECT reconstruction *Phys. Med. Biol.* **61** 4300–15

Van Audenhaege K, Van Holen R, Deprez K, Karp J S, Metzler S and Vandenberghe S 2011 Design of a static full-ring multi-pinhole collimator for brain SPECT *IEEE Nuclear Science Symp. and Medical Imaging Conf. Record*

Van Audenhaege K, Vandenberghe S, Deprez K, Vandeghinste B and Van Holen R 2013 Design and simulation of a full-ring multi-lofthole collimator for brain SPECT *Phys. Med. Biol.* **58** 6317–36

van der Have F, Vastenhouw B, Ramakers R M, Branderhorst W, Krah J O, Ji C, Staelens S G and Beekman F J 2009 U-SPECT-II: an ultra-high-resolution device for molecular small-animal imaging *J. Nucl. Med.* **50** 599–605

van der Have F, Vastenhouw B, Rentmeester M C M and Beekman F J 2008 System calibration and statistical image reconstruction for ultra-high resolution stationary Pinhole SPECT *IEEE Trans. Med. Imaging* **27** 960–71

Van Laere K, Koole M, Kauppinen T, Monsieurs M, Bouwens L and Dierck R 2000 Nonuniform transmission in brain SPECT using 201 Tl, 153 Gd, and ^{99m}Tc static line sources: anthropomorphic dosimetry studies and influence on brain quantification *J. Nucl. Med.* **41** 2051–63

Vastenhouw B and Beekman F 2007 Submillimeter total-body murine imaging with U-SPECT-I *J. Nucl. Med.* **48** 487–93

Wang B, Van Roosmalen J, Piët L, VanSchie M A, Beekman F J and Goorden M C 2017 Voxelized ray-tracing simulation dedicated to multi-pinhole molecular breast tomosynthesis *Biomed. Phys. Eng. Express* **3** 045021

Zubal I G, Harrell C, Smith E, Rattner Z, Gindi G and Hoffer P 1994 Computerized three-dimensional segmented human anatomy *Med. Phys.* **21** 299–302